Seamounts generate efficient active transport loops to nourish the twilight ecosystem

Xinyang Wang, Hongliang Li, Jingjing Zhang, Jianfang Chen, Xiaohui Xie, Wei Xie, Kedong Yin, Dongsheng Zhang, Diana Ruiz-Pino, Shuh-Ji Kao

OCEANOGRAPHY

Seamounts generate efficient active transport loops to nourish the twilight ecosystem

Xinyang Wang[1,2,3], Hongliang Li[1,2]*, Jingjing Zhang[1,2], Jianfang Chen[1,3,4]*, Xiaohui Xie[4], Wei Xie[2,5], Kedong Yin[2,5], Dongsheng Zhang[1,2,3], Diana Ruiz-Pino[6], Shuh-Ji Kao[7]

Seamounts are ecological oases nurturing abundant fisheries resources and epibenthic megafauna in the vast oligotrophic ocean. Despite their significance, the formation mechanisms underlying these seamount ecological oases remain uncertain. To shed light on this phenomenon, this study conducted interdisciplinary in situ observations focusing on a shallow seamount in the oligotrophic ocean. The findings show that the seamount's topography interferes with the oceanic current to generate lee waves, effectively enhancing the nutrient supply to the euphotic layer downstream of the seamount. This continuous supply enhances phytoplankton biomass and subsequently the grazing and diurnal vertical migration of zooplankton, rapidly transporting the augmented phytoplankton biomass to the aphotic layer. Unlike the cyclonic eddies that move in the upper ocean, seamounts stand at fixed locations creating a more efficient and steady active transport loop. This active transport loop connects the euphotic and twilight zones, potentially conveying nourishment to benthic ecosystems to create stereoscopic oases in the oligotrophic ocean.

INTRODUCTION

Oligotrophic oceans with extremely low chlorophyll *a* (Chl-*a*) (<0.1 mg m^{-3}) (*1*) occupy more than 25% of the global ocean (*2*). They are regarded as ecological deserts (*2*, *3*) due to the lack of essential nutrients required for phytoplankton growth in the euphotic zone. The mesopelagic and bathypelagic ecosystems, which depend on the detritus inputs originating from primary producers in the upper layers, experience food limitation because of low export of organic matter, particularly in oligotrophic oceans with the low primary production aggravated by low export efficiency (*4*). Amid these conditions, nearly half of the world's seamounts (16,760 seamounts) are dispersed across oligotrophic oceans, potentially serving as hotspots for marine biodiversity and fisheries resources (*5*–*9*). Many seamounts function as ecological oases and provide habitats for numerous endemic species, and the fishing catch tends to increase close to these seamounts (*6*, *10*). Although the importance of seamounts is well recognized from different aspects, the underlying mechanisms for the formation of seamount ecological oases, particularly regarding their nourishment sources, remain uncertain (*7*–*9*) and subject to considerable debate.

Seamounts rise sharply from the ocean floor, piercing the aphotic zone (depths below 1000 m), with 15.4% of seamounts reaching into the twilight zone (200 to 1000 m) and 5.0% of seamounts being shallow seamounts that extend into the euphotic zone (<200 m). As natural obstacles to the oceanic current, seamounts can modulate hydrological characteristics at regional and global scales (*11*). The depth of the seamount's summit stands out as the most crucial factor influencing the intensity of upper-layer physical and ecological responses, with shallow seamounts typically exhibiting more pronounced reactions (*9*, *12*). Existing observations and numerical simulations have captured the changes in thermodynamic structures and mixing intensity induced by seamounts (*13*–*22*) through processes such as lee waves. These changes substantially improve nutrient availability within the euphotic zone, consequently stimulating primary productivity (*7*), which has been confirmed by extensive field and satellite observations *(12, 14, 23–27)*. In the mesopelagic and bathypelagic zones, seamounts also attract gatherings of migratory animals, such as tuna and sharks (*28*, *29*), and host remarkably species-rich benthic ecosystems (*30*). A common consensus is that there is an intrinsic connection between the enhanced primary production and the formation of mesopelagic-bathypelagic ecological oases (*31*, *32*). The biological carbon pump, including the production of organic matter through phytoplankton photosynthesis, and subsequent export to deep layers through various pathways, may provide the main food and energy for communities in the twilight and aphotic zones (*33*–*35*). Hence, the intensity and quality of delivered organic matter can directly regulate the size, structure, and function of deeper communities (*33*, *36*). However, how and by what this connection is built remains unclear because of the lack of comprehensive observations.

To uncover the formation mechanisms of seamount ecological oases, it is crucial to understand the dynamics of production processes and the export pathways of particulate organic matter along the flow course under the influence of topography. Therefore, this study selected a shallow seamount (Xianbei seamount with a summit of ~208 m) in the oligotrophic central South China Sea (SCS) for comprehensive field observations, and the findings could potentially apply to other shallow seamounts in oligotrophic oceans. Through cross-sectional and diurnal observations, this study unveiled the asymmetry in organic matter production and export between the upstream and downstream sides, primarily driven by lee waves and a zooplankton-mediated active transport loop. These asymmetries provide direct evidence that the intense active transport loop can rapidly transport enhanced primary production to the deep layer on the downstream side, ensuring a consistent food supply for deep ecosystems

[1]Key Laboratory of Marine Ecosystem Dynamics, Second Institute of Oceanography, Ministry of Natural Resources, Hangzhou, China. [2]Southern Marine Science and Engineering Guangdong Laboratory (Zhuhai), Zhuhai, China. [3]School of Oceanography, Shanghai Jiao Tong University, Shanghai, China. [4]State Key Laboratory of Satellite Ocean Environment Dynamics, Second Institute of Oceanography, Ministry of Natural Resources, Hangzhou, China. [5]School of Marine Sciences, Sun Yat-sen University, Zhuhai, China. [6]Sorbonne University (S.U.), CNRS-IRD-MNHN, LOCEAN Laboratory/IPSL, Paris, France. [7]State Key Laboratory of Marine Resource Utilization in South China Sea, Hainan University, Haikou, China.
*Corresponding author. Email: lihongliang@sio.org.cn (H.L.); jfchen@sio.org.cn (J.C.)

and potentially contributing to the formation of stereoscopic oases around seamounts.

RESULTS AND DISCUSSION

Lee waves promote phytoplankton biomass downstream

The Xianbei seamount is a steep seamount (3800 m in height) with a shallow summit depth (208 m below the sea surface) that is influenced by the southwest monsoon circulation (Fig. 1A). The current above 200 m was found to be northeasterly, with an average velocity of 0.26 m s^{-1} observed using lowered acoustic Doppler current profilers (LADCP) (Fig. 1B). The surface water was warm and fresh, and the maximum salinity occurred at the subsurface layer (fig. S1), showing the characteristics of tropical open oceans with strong stratification (Fig. 2A) (*37*). When the current passed over the summit, the depression and jump of isotherms were observed on the downstream side, presenting the typical characteristics of lee waves (*18*). The lee wave Froude number on the Xianbei seamount of $\varepsilon_s = \frac{Nh}{U} \sim 100 \gg 1$ ($N \sim 10^{-2}$ s^{-1}, $U \sim 0.26\,m\,s^{-1}$, $h \sim 3800$ m) indicated that the lee waves were highly nonlinear and prone to breaking, thereby enhancing turbulent mixing (*38*). In this condition, the topographic interference resulted in a dynamic physical environment downstream. The Thorpe scale method was used to estimate the turbulent dissipation rate ε and diapycnal diffusivity K_ρ. The results indicated that the average ε and K_ρ of the water column (above 300 m) at the time-series stations on the summit (ε: 5.15×10^{-8} W kg^{-1}; K_ρ: 4.63×10^{-5} m^2 s^{-1}) and the downstream slope (ε: 6.65×10^{-8} W kg^{-1}; K_ρ: 9.80×10^{-5} m^2 s^{-1}) were both roughly twice as high as that on the upstream slope of the seamount (ε: 2.74×10^{-8} W kg^{-1}; K_ρ: 2.43×10^{-5} m^2 s^{-1}). In particular, the intensified ε and K_ρ values at 200 to 300 m on the downstream side may indicate enhanced mixing in the deep layer (Fig. 2, E and F). This enhanced mixing could be attributed to the fragmentation of the lee wave, which served as the primary source of turbulent energy on the downstream slope (*18*). Such a change in the dynamics corresponded to the oscillations of the nitracline (see below), which could improve nutrient availability.

The surface ocean surrounding Xianbei was reported to be nutrient-depleted in summer (*39*, *40*), consistent with the observations in the present study. The observational transect in this work showed that the nitracline (represented by 0.5 μmol kg^{-1} isolines) generally coincided with the thermocline (*D*22, depth of 22°C isotherm) (Fig. 2, A and B), and the nitracline rose from approximately 105 m deep at the reference station (A6) to 65 to 85 m deep around the summit and downstream (Fig. 2B and fig. S2). This isopycnic elevation allows more of the subsurface nitrate-rich water to rise into the interior of the euphotic zone, effectively increasing the

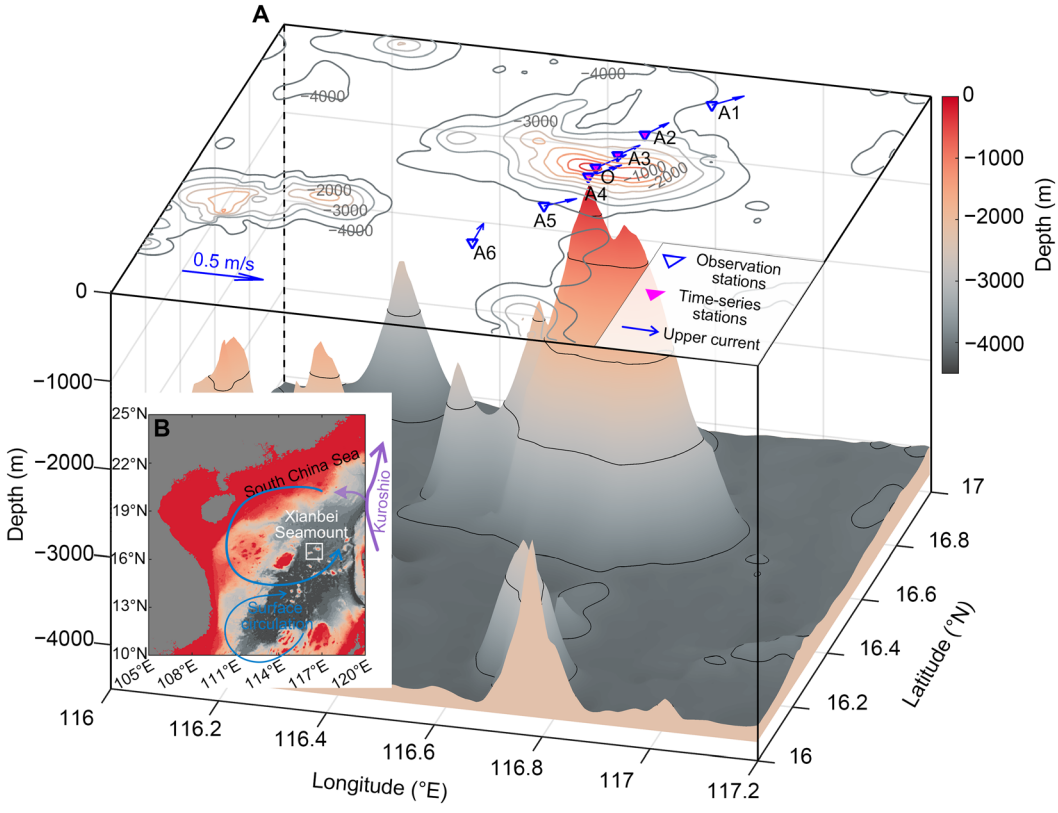

Fig. 1. Geographical location and topography of Xianbei seamount. (**A**) The white box on the map represents the location of Xianbei seamount (116.45° to 117.00°E, 16.42° to 16.80°N), and the solid lines delineate the prevailing circulation patterns observed from 14 to 24 September 2021. (**B**) A three-dimensional topographic map of Xianbei seamount and the upper 200-m current observed using LADCP is presented. The observation stations are indicated by blue inverted triangles on the map, with four pink-filled symbols representing the time-series stations. On the topographic plane, blue arrows depict the upper current, while the contours illustrate the isobaths with labels indicating their respective depths. The observation transect is approximately parallel to the direction of the current. The bottom topography of the Xianbei seamount is obtained from global bathymetry data with a 15–arc sec resolution (*72*).

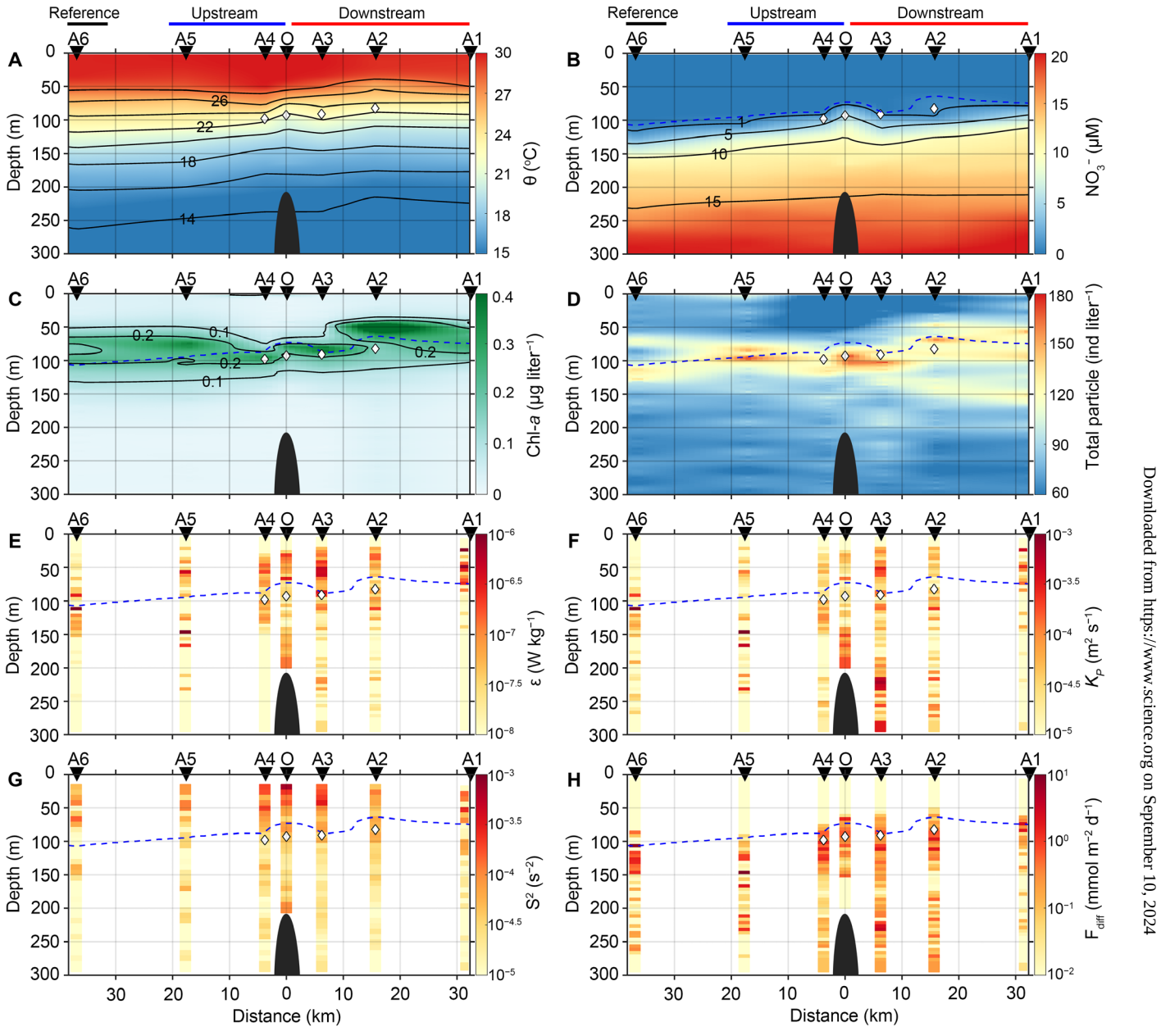

Downloaded from https://www.science.org on September 10, 2024

Fig. 2. Sectional distribution of the hydrographic, kinetic, and biochemical parameters of the parallel section in the upper 300 m. (**A**) Potential temperature θ (°C), (**B**) NO_3^- (μmol L^{-1}), (**C**) Chl-*a* (mg m^{-3}), (**D**) particle concentration (ind L^{-1}), (**E**) turbulent kinetic energy dissipation rate ε (W kg^{-1}), (**F**) diapycnal diffusivity K_ρ (m^2 s^{-1}), (**G**) vertical shear square S^2 (s^{-2}), and (**H**) NO_3^- flux F_{diff} (mmol m^{-2} d^{-1}). In each panel, the observation stations are represented by inverted triangles at the top, and the shades of black indicate the summit of the seamount. In (B) to (H), the nitracline is represented by the blue dashed lines. The vertical shear square S^2 was calculated as $S^2 = \left(\frac{\partial u}{\partial z}\right)^2 + \left(\frac{\partial v}{\partial z}\right)^2$. At the top of the image, the labels "Reference," "Upstream," and "Downstream" indicate the reference station, the upstream side, and the downstream side of the seamount, respectively. In each panel, the black rhomboids represent the depth of the euphotic layer (Z_{eu}). The Z_{eu} is not displayed for stations for which photosynthetically active radiation (PAR) data are unavailable.

nitrate availability at the summit and downstream side of the seamount. The nitrate reservoir in the upper 100-m water column for the summit (O), downstream slope (A3) and downstream bottom (A2) were found to be 35.4 ± 15.6, 22.2 ± 15.9, and 33.4 ± 12.8 mmol m^{-2}, respectively, while the nitrate reservoir on the upstream slope (A4) was only 17.5 ± 11.1 mmol m^{-2}. Besides, the average nitrate diffusive flux F_{diff} around 75 to 100 m on the downstream slope (A3) and bottom (A2) were 0.32 ± 0.21 and 0.57 ± 0.47 mmol m^{-2} d^{-1}, respectively, which were higher than the value of 0.25 ± 0.18 mmol m^{-2} d^{-1} observed on the upstream slope (fig. S2). Obviously, the fragmentation of the lee wave increased the diapycnal diffusive nitrate across the base of the euphotic layer.

The vertical transect of Chl-*a* exhibited characteristics that were typical for the oligotrophic ocean, featuring an extremely low Chl-*a* concentration at the surface and a subsurface Chl-*a* maximum (SCM) (Fig. 2C and Fig. 3, E to H) (*41*). The depth of the SCM (DCM)

downstream reflected shoaling consistent with the shoaling of the nitracline (Fig. 2, B and C). Both the depth-integrated Chl-*a* (*t* test, $P < 0.05$) and the mean particle concentration (*t* test, $P < 0.01$) above the depth of the euphotic layer (Z_{eu}) increased significantly relative to that of upstream (fig. S3). Although increased production has also been observed on other seamounts (*23*–*25*, *42*–*44*), the highlight of this study lies in quantitatively assessing the nutrient supply intensity based on nitrate reservoirs and diffusion fluxes. The tight correlation between the DCM and the nitracline ($r = 0.73$, $P < 0.01$), as well as the proximity of the lower boundary of the SCM layer to the nitracline (Fig. 2, B and C), also suggests a spatial coupling between the nutrient supply from the subsurface and the primary

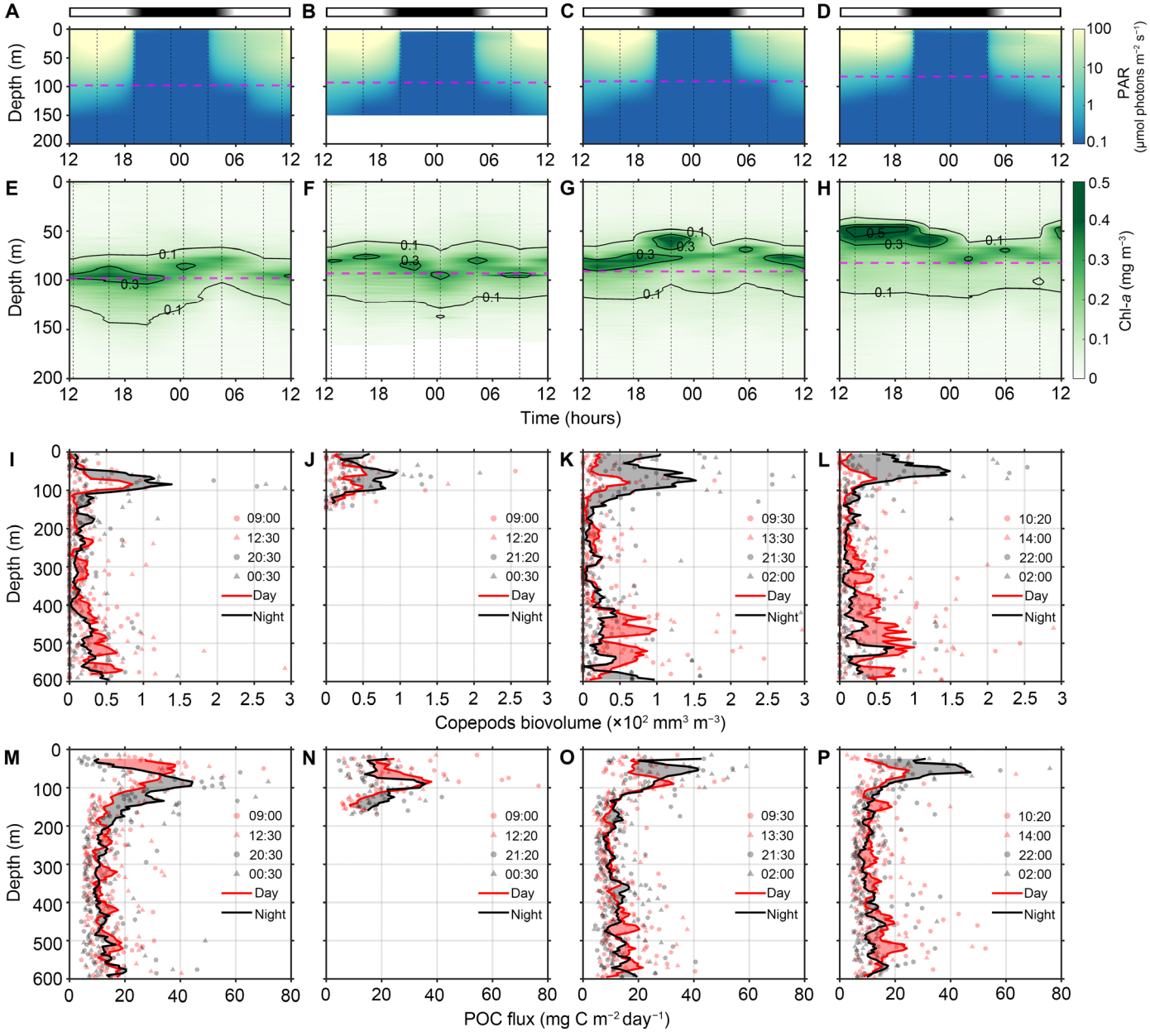

Fig. 3. Temporal variations of the PAR intensity (μmol photons m^{-2} s^{-1}), Chl-*a* (mg m^{-3}), the copepod zooplankton biovolume (×10^2mm^3 m^{-3}), and the estimated POC flux (mg C $m^{-2}d^{-1}$). (**A** to **D**) The panels in the first row respectively represent the diurnal variations in PAR at the upstream slope A4 (A), the summit O (B), the downstream slope A3 (C), and the downstream bottom A2 (D). (**E** to **H**) The diurnal variations of Chl-*a* at stations A4 (E), O (F), A3 (G), and A2 (H). (**I** to **L**) The diurnal variations of the POC flux at the four time-series stations. (**M** to **P**) The diurnal variations of copepod biovolume at the four time-series stations. The figure exhibits four horizontal bars positioned at the top, signifying the diurnal variations. In (A) to (H), the dotted black lines correspond to the observation time, and the pink dashed lines indicate the Z_{eu}. In (I) to (P), the gray and red symbols represent the observation results in 5-m bins, while the black (red) solid lines represent the five-point running average during nighttime (daytime). The shaded area in (I) to (P) represents the difference between daytime and nighttime, with red indicating higher values during daytime compared to nighttime, and gray indicating the opposite, where nighttime values are higher than daytime values. In addition, in each panel, the time refers to the local time (UTC +08:00).

productivity above the Z_{eu}. All the above features and correlations indicate that seamounts enhance the availability of nutrients downstream to increase the phytoplankton biomass and production.

Enhanced zooplankton migration and feeding on phytoplankton

This work found that the intense dynamic physical processes downstream stimulated not only the primary production but also the zooplankton feeding on phytoplankton. First, except for the summit, the SCM was at the lowest level of the day around dawn for all four time-series stations (Fig. 3, E to H). This phenomenon implied nocturnal feeding by zooplankton. In addition, the diurnal variability in the depth-integrated Chl-*a* above the Z_{eu} (A2: 10.46 ± 4.16 mg m^{-2}; A3: 10.03 ± 2.40 mg m^{-2}) and the SCM (A2: 0.45 ± 0.15 mg m^{-3}; A3: 0.41 ± 0.08 mg m^{-3}) were more pronounced downstream relative to that upstream (depth-integrated Chl-*a*: 7.88 ± 1.40 mg m^{-2}; SCM: 0.36 ± 0.06 mg m^{-3}) (fig. S3). The particle concentrations also showed similar diurnal variations (fig. S4). It was highly likely that these differences in diurnal variations were caused by the variances in feeding intensity.

The Underwater Version Profiler 5 (UVP)–obtained particle images were processed using automated identification and manual verification methods to obtain the quantity and size information for copepods zooplankton (see Materials and Methods). Subsequently, the abundance and biovolume of copepods were calculated (Fig. 3, I to L, and figs. S4 and S5). The diurnal vertical migration (DVM) behavior enabled migrating zooplankton to feed on the phytoplankton of the euphotic zone. During the nighttime, the copepod biovolume above 200 m was higher relative to that during the daytime (Fig. 3 and fig. S4). Such a temporal pattern explained the low Chl-*a* around dawn. These nocturnal feeding patterns allowed the growth and reaccumulation of phytoplankton during the daytime. In addition, the copepod biovolume was notably higher downstream, resulting in more intense DVM behavior being observed at the downstream stations as the daytime and nighttime profiles were separately integrated (Fig. 3). The biovolume involved in diurnal migration was estimated on the basis of the difference of zooplankton biovolume in the upper water column. The estimated migrating zooplankton biovolume on the downstream side was 1.5 (A2, 2.14 cm^3 m^{-2}) and 2.0 (A3, 2.82 cm^3 m^{-2}) times greater than that on the upstream side (A4, 1.39 cm^3 m^{-2}), respectively, constituting 67.3% (A2) and 70.3% (A3) of the total biovolume during the nighttime. In comparison, only 52.5% of zooplankton on the upstream side exhibited diurnal migration. Spatial variations in diurnal zooplankton migration were also supported by evidence from the acoustic backscatter intensity of 300 kHz LADCP (the size range of scatters >1 mm was consistent with the size range of copepods identified using UVP; fig. S6) for the upper 600-m water column. Under the circumstance of an abundant nutrient supply to the euphotic layer downstream of the seamount, the interplay of the diurnal cycle between zooplankton and phytoplankton creates a factory that efficiently reproduces and consumes solar energy–based organics.

Active transport loop facilitates efficient organic matter export

In addition to satisfying their own nutritional needs, zooplankton can transport organic matter to the depth during diurnal migration and excrete in the depth in a process known as the active export flux, which can enhance the efficiency of the biological carbon pump (*45*, *46*). The estimated flux of particulate organic carbon (POC) calculated using the carbon-based particle size approach in the epipelagic and mesopelagic layers exhibited diurnal variations and downstream enhancement similar to those of copepods (Fig. 3, I to P). The average POC flux above 200 m downstream during the daytime decreased by 6.9 mg C m^{-2} d^{-1} (A2) and 7.2 mg C m^{-2} d^{-1}(A3) compared to nighttime, which were values 2.9 and 3.0 times greater, respectively, than those of the upstream (A5: 2.4 mg C m^{-2} d^{-1}). In contrast, the average POC flux in the 400- to 600-m water column during the daytime exhibited increases of 3.0 mg C m^{-2} d^{-1}(A2) and 2.6 mg C m^{-2} d^{-1}(A3), which were 2.3 and 2.0 times higher than that of upstream station (A5: 1.3 mg C m^{-2} d^{-1}), respectively. The almost identical diurnal variations of POC flux and copepod biovolume indicate that the feeding and delivery effects of migrators dominate the diurnal variations of the POC flux.

Observing the active export flux poses substantial challenges. With the assumption that the passive POC sinking flux driven by gravity was consistent, this study evaluated the active POC flux derived from the migrating zooplankton based on the integral of the day-night POC flux difference between 400 and 600 m (Fig. 3, M to P), which could be ingested at the epipelagic layer and carried downward to the mesopelagic layer to be excreted in the form of fecal pellets by migrants (*47*, *48*). It was estimated that active transport contributed an additional 24% (A2) and 20% (A3) of the fresh POC flux on the downstream side. The time-series observations offered valuable direct evidence regarding the DVM of zooplankton and the crucial role of particle delivery, illustrating the feeding process in the epipelagic layers and excretion in the mesopelagic layers. These findings suggest that under the delivery effect of migrators, more POC accumulates in the mesopelagic zone on the downstream side rather than being retained inside the euphotic zone as it is upstream. The active POC flux bypassing the microbial degradation and intense remineralization processes could be much fresher than the negative POC flux, which exhibits a slow sinking rate and high degradation degree (*46*, *49*).

The augmentation of the surface net primary production typically contributes to the intensified export of organic carbon to the deep ocean (*50*), in which the active export facilitated by the DVM of zooplankton plays a pivotal role. Recent reports also suggest a higher proportion of active flux in the high-productivity regions of the tropical and subtropical Atlantic oceans (*45*). Despite persistent skepticism regarding whether the transiently enhanced primary production can be transferred to higher trophic levels in seamount ecosystems (*51*, *52*), the present investigation has unveiled that the synergy between the seamount-induced enhancement of primary production and the intense DVM of zooplankton can constitute an efficient active transport loop. The pivotal propulsion driving this active transport loop arises from the migrating zooplankton, while the enhanced primary production serves as the principal cargo (Fig. 4). Through the combined effects of a continuous supply of primary production and regular diel vertical migration in seamounts, this loop perpetually and rhythmically transports a substantial amount of organic matter into the deep ecosystems. Compared to the oligotrophic SCS basin where the Xianbei seamount is located, the POC flux at 500-m depth in the seamount region is approximately 2.6 times higher than that of the basin (Fig. 5c and fig. S7). Moreover, the observations in the present study also indicated that the active transport loop driven by lee waves and DVM exhibited spatial asymmetry, specifically in terms of the different responses between the upstream and downstream sides of the seamount (Fig. 4).

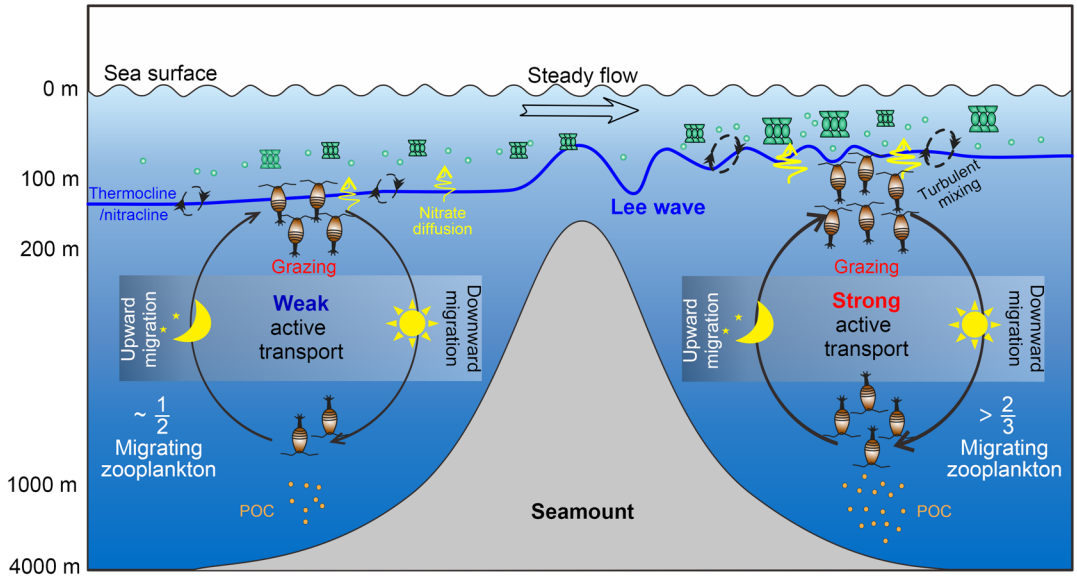

Fig. 4. Schematic illustrations of an efficient active transport loop for organic carbon. The interaction between the flow and the steep topography of the seamount leads to the formation of a lee wave (indicated by the blue line), which is typically characterized by thermocline/nitracline jumps on the downstream side of the seamount. The turbulent mixing (indicated by black dotted lines) is intensified on the downstream side, primarily due to the breaking of the lee wave, which in turn enhances the pulsed injection of nutrients into the euphotic layer. Compared with the reference stations and the upstream side, the increased nutrient injection contributes to the growth of phytoplankton and the accumulation of POC on the downstream side. Furthermore, the diel vertical migration on the downstream side is more intense, leading to pronounced feeding and transport effects on POC. These processes collectively form the efficient active transport loop associated with seamounts. Consequently, the enhanced primary production downstream can be actively exported to the twilight zone by the DVM in a diurnal cycle, which will supply more and fresher food sources for the mesopelagic and benthic biotic community.

Seamounts create stereoscopic oases in the oligotrophic ocean

Satellite Chl-*a* observations showed that approximately 45% of seamounts with summits shallower than 100 m and 23% of seamounts shallower than 500 m in the western Pacific Ocean exhibited long-term, significant Chl-*a* enhancement (*12*). For the oligotrophic ocean, the productivity-enhanced seamount areas, similar to islands (*53*, *54*), scatter surface ecological oases across a two-dimensional perspective. The observations in the present study reveal that the enhanced primary production in the euphotic zone serves as the initial segment (organic pool) of the active transport loop, which is performed by zooplankton collecting nutrition from the epipelagic layers during the nighttime and transporting nutrition downward to nourish the twilight ecosystems during the daytime. This creates a fixed hotspot delivering food supported by solar energy to deep ecosystems, potentially aggregating predators in the mesopelagic zone and benthic organisms in the bathypelagic system (*7*, *9*). Under the continuous action of the active transport loop at a fixed location, the surface oases extend spatially from the euphotic zone downward into the mesopelagic-benthic zone via the daily traffic channel of zooplankton, thus creating three-dimensional stereoscopic ecological oases for the upper 600 m on the vertical scale and more than 30 km on the horizontal scale.

To more intuitively assess the high POC flux, we provided a comparative example between a typical oligotrophic region, the NPSG region (North Pacific Subtropical Gyre), and the Xianbei seamount. The NPSG region is one of the typical oligotrophic regions with a high seamount density, and, according to statistics, the NPSG region harbors 2910 seamounts. Among these, 211 seamounts have summit depths equivalent to or shallower than the Xianbei seamount in the present study (Fig. 5). As a shallow seamount, the Xianbei seamount exhibited a POC flux at 500-m depth over 2.8 to 5.1 times higher than that of the NPSG region (Fig. 5C). Assuming that shallow seamounts can generate POC flux similar to that of the Xianbei seamount, it was estimated that a mere 0.74% of the area (see Materials and Methods) occupied by shallow seamounts might contribute up to 2.1 to 3.8% of the total POC flux in the NPSG region. Their locally sustained and intense organic matter export could provide the food supply necessary for seamounts to function as important ecological oases within the oligotrophic ocean. Recent field observations have also revealed that obvious seamount effects exist in some deep-sea seamounts (*55*), prompting further exploration into these potentially overlooked ecological hotspots within the vast deep ocean.

In oligotrophic oceans, processes such as eddies can trigger nutrient replenishment and enhanced primary production (*56*, *57*). However, eddies are less likely to form oases due to their mobility and short lifespan (*58*). Islands, as another type of oasis, can also substantially increase the phytoplankton biomass and marine food resources through numerous similar physical processes shared with seamounts (*53*). However, a notable distinction between seamounts and islands lies in the fact that islands protrude above the sea surface, whereas seamounts remain submerged. This distinction potentially results in differences in the nearshore ecosystems around islands and seamounts. For example, the exposed land on islands provides more suitable habitats for seabirds, and seabird guano can subsidize nutrients for nearshore biological communities (*59*). The stereoscopic ecological oases formed by seamounts and islands provide irreplaceable ecological connectivity (*60*), fisheries resources (*5*, *10*), and marine migration corridors (*61*) in oligotrophic oceans. The findings of the present study on seamounts can also offer crucial reference value for

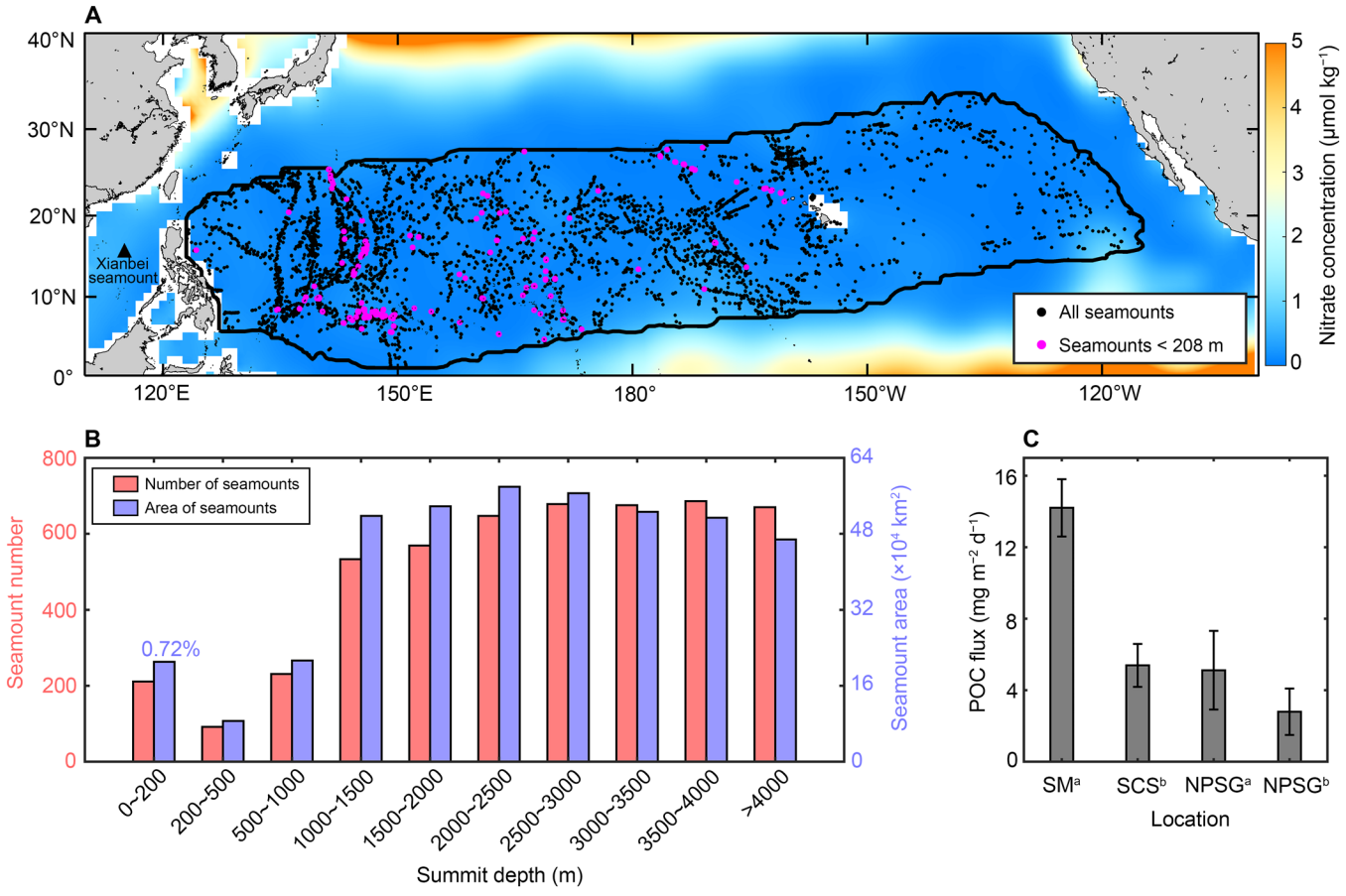

Fig. 5. Distribution of seamounts and summit elevation distribution in the NPSG. (**A**) Spatial distribution of the seamounts in the NPSG region. The background color represents the surface nitrate concentration from the World Ocean Atlas 2018, and the solid black line indicates the range of NPSG based on the surface Chl-*a* concentration <0.1 mg m^{-3} (*2*). Black dots represent all seamounts in the NPSG region, and pink dots represent seamounts with summit depths shallower than 208 m. (**B**) The number and proportion of seamounts with different summit depths in the NPSG region. Red bars represent the number of seamounts at different depths, while blue bars represent the total area of different seamounts. The number of seamounts with summit depths shallower than 208 m accounts for 7.2% of the seamount count in this region, covering only 0.74% of the NPSG area. (**C**) Comparison of the POC flux at 500-m depth between the Xianbei seamount (SM), the South China Sea (SCS) basin, and the NPSG region. Here, the POC fluxes in the NPSG region were obtained on the basis of available UVP data (labeled as "a") (*73*) and aggregated direct observations by sediment traps (labeled as "b") (*74*, *75*). The POC flux in the SCS basin was 5.39 ± 1.20 mg C m^{-2} d^{-1}, which is also observed by the sediment trap at 500-m depth (fig. S7). The shallow seamount exhibits a POC flux 2.8 to 5.1 times (due to different observation instruments) higher than that of the NPSG region, and all shallow seamounts might contribute up to 2.1 to 3.8% of the total POC flux in the NPSG region. The statistics on seamount distribution, quantification, and area are based on the publicly available global seamount database (*71*).

exploring the more complex mechanisms driving the formation of island oases.

MATERIALS AND METHODS

Study area characteristics and observation scheme

Xianbei seamount is located in the central SCS basin, surrounded by a flat ocean floor with a depth of about 4000 m. The seamount is an isolated and steep shallow seamount with a summit elevation of 208 m, and the average bottom topography slope is greater than 15°, as shown in fig. S8. The transverse section of the seamount is roughly elliptical, with a long axis of about 60 km and a short axis of 40 km. Field observations were conducted onboard the R/V *ShenKuo* from 14 to 24 September 2021, and a section parallel to the flow direction was designed to conduct comprehensive field observations (Fig. 1). This section could be divided into upstream and downstream sides according to the current direction and the position of the summit. Four time-series stations were set longitudinally from upstream to downstream. The four time-series stations stretched about 25 hours with an interval of 4 hours, located at the upstream slope (A4), summit (O), downstream slope (A3), and downstream bottom (A2) (Fig. 1). A station (A6) farther upstream was considered as the reference station outside the seamount.

The temperature, salinity, depth, fluorescence, and nitrate were measured using a Seabird 911 plus CTD sensor (frequency, 24 Hz) equipped with a fluorometer and Seabird Deep-Suna (1 Hz). The photosynthetically active radiation (PAR) was measured with a PAR sensor. The current and particle size spectrum were derived from an RDI 300 kHz LADCP and UVP5 (maximum frequency, 20 Hz), respectively. These instruments were mounted to the CTD rosette and deployed synchronously at a lowering speed of ~0.35 m s^{-1}. The thermocline depth was defined as the depth of the 22°C isotherm. The

nitracline depth was derived as the depth of the isoline of 0.5 μmol kg^{-1}, and the depth with 1% of the surface PAR was defined as the depth of the euphotic layer (Z_{eu}).

Turbulent mixing and diffusive nitrate flux

The Thorpe-scale method was used to evaluate the strength of the mixing with reference to the mature data processing procedure (*62*). Before applying the Thorpe-scale method for calculation, the original CTD data underwent preprocessing through a standardized procedure. This involved using Seabird processing software to perform tasks such as minimizing thermal lag, removing salinity spiking, identifying occasionally reversed signs, eliminating extremely abnormal data points, and averaging at regular depth intervals. The Thorpe scale L_T is a measure of the vertical length scale of density overturns generated by turbulence in a stratified water column for a potential density profile. The L_T is calculated as

$$L_T = \sqrt{\overline{d'^2}} \tag{1}$$

where the *d*' is the Thorpe displacement representing the vertical distance from the current depth of a water parcel after turbulent overturning (d_f) to the original depth where the same water parcel should be in a stable stratified water column (d_i) (*63*).

The turbulence dissipation rate ε can be estimated on the basis of the Thorpe scale and the stratification as follows

$$\varepsilon = a \cdot {L_T}^2 \cdot N^3 \tag{2}$$

where $a = 0.8$ is a constant of proportionality (*64*) and N is the buoyancy frequency, calculated as $N^2 = \frac{g}{\rho} \times \frac{\partial \rho}{\partial z}$, where g is the gravity and ρ_0 is the constant reference density. Then, the diapycnal diffusivity K_ρ can be calculated as follows

$$K_\rho = \Gamma \cdot \frac{\varepsilon}{N^2} \tag{3}$$

where Γ is the mixing efficiency and is typically taken to be 0.2 (*65*). Last, according to Fick's law, the vertical nitrate gradient $\frac{\partial c}{\partial z}$ and the diapycnal diffusivity K_ρ were multiplied to estimate the vertical turbulent nitrate flux F_{diff}. The equation is as follows

$$F_{diff} = -K_\rho \times \frac{\partial c}{\partial z} \tag{4}$$

where the $\frac{\partial c}{\partial z}$ is positive downward and the F_{diff} is positive upward.

Copepod zooplankton abundance and biovolume

The UVP5 HD allows for the in situ quantifications of all objects >100 μm, including both nonliving particles and living organisms (i.e., zooplankton), with high vertical resolution (*66*). The size and gray level of every object larger than 100 μm were recorded, but only objects larger than 600 μm were stored as images in the instrument for subsequent analysis. The recorded volume of each image was 1.02 liter, and the conversion equation from pixel area to size was $S_m = 0.003 S_p^{1.3348}$, where the S_p was the particle area in pixels and S_m was in mm^2. After the instrument was retrieved, all images >600 μm were extracted using the ImageJ-based ZooProcess macro set and uploaded to Exotaxa website (http://www.ecotaxa.cn/) for the automated classification, and the classifications were validated by experts. Thus, the size information was obtained for each particle and each copepod zooplankton, and the volume of each object was calculated on the basis of the equivalent sphere diameter *d* as follows

$$V = \frac{4}{3}\pi \times \left(\frac{d}{2}\right)^3 \tag{5}$$

Last, by summing the quantities and volumes of particles and copepod zooplankton based on observed water column volumes, this work derived the concentrations of particles and the abundance and biovolume of copepod zooplankton. The abundance and biovolume of the copepod zooplankton were both binned into 5-m intervals for further analysis.

POC flux estimation based on UVP particle size spectrum

The POC flux was estimated on the basis of the carbon-based particle size approach (*67*–*69*). The distribution of particle size follows a power law in particle size ranging from micrometers to millimeters (*70*). The POC flux corresponded to the flux spectrum integrated over all particles from the smallest particle size (d_{min}) to the largest size (d_{max}) as follows:

$$POC\ flux = \int_{d_{min}}^{d_{max}} n(d) \cdot m(d) \cdot \omega(d) \cdot dd \tag{6}$$

where $n(d)$ is the particle size spectrum (*67*).

In the actual calculation process, the POC flux was integrated using Eq. 6. Both mass *m(d)* and settling rate *w(d)* are functions of the particle diameter *d*, and the product of *m(d)* and *w(d)* can be expressed as a power law function of *d*, namely $m(d) \times w(d) = Ad^B$. Therefore, Eq. 6 can be transformed into:

$$POC\ flux = \sum_{i=1}^{x} n_i\, A d_i^B \cdot d_i \tag{7}$$

where $A = 12.5 \pm 3.40$ mg m^{1-B} d^{-1}, and $B = 3.81 \pm 0.70$. Parameters *A* and *B* were derived using the minimization procedure to find the best fit between the two fluxes estimated on the basis of sediment traps widely distributed around the global ocean and derived on the basis of the UVP particle size distribution, respectively (*67*). The POC flux estimated on the basis of the particle size spectrum was also binned into 5-m intervals. For the time-series stations, the estimated POC fluxes during daytime and nighttime were averaged with the observation results from 08:00 to 17:00 and 20:00 to 05:00 (local time), respectively, and each period contained at least two profile observations. It was estimated that the proportion of living zooplankton to the total particle volume was less than 10% (fig. S9), indicating that the living zooplankton did not substantially affect the overall trend of passive export. Nevertheless, to ensure a more precise evaluation of the passive flux, this study relied on nighttime POC flux profiles. Simultaneously, the variance between daytime and nighttime POC fluxes within the 400- to 600-m water columns was leveraged to quantify the intensity of active transport.

Global seamount dataset

The global seamount data used in this study were obtained from the second version of the seamount dataset (*71*). This dataset was compiled on the basis of version 11 of the Shuttle Rodar Topography Mission "SRTM30 plus" global bathymetry, encompassing information on the locations, area, height, and elevation of 37,889 seamounts worldwide. There are 211 seamounts located in the NPSG region with

summit depths shallower than that of the Xianbei seamount. On the basis of the area data from the global seamount dataset, the total area of these seamounts was calculated, accounting for 0.74% of the total area of the NPSG region (2.91×10^7 km^2) (*2*). In addition, on the basis of the location information within this dataset, seamounts with an average surface Chl-*a* concentration below 0.1 mg m^{-3} were classified as oligotrophic seamount regions (fig. S10).

Supplementary Materials

This PDF file includes:

Figs. S1 to S10
References

REFERENCES AND NOTES

1. D. Antione, J.-M. André, A. Morel, Oceanic primary production: 2. Estimation at global scale from satellite (coastal zone color scanner) chlorophyll. *Global Biogeochem. Cycles* **10**, 57–69 (1996).
2. M. Dai, Y. W. Luo, E. P. Achterberg, T. J. Browning, Y. Cai, Z. Cao, F. Chai, B. Chen, M. J. Church, D. Ci, C. Du, K. Gao, X. Guo, Z. Hu, S. J. Kao, E. A. Laws, Z. Lee, H. Lin, Q. Liu, X. Liu, W. Luo, F. Meng, S. Shang, D. Shi, H. Saito, L. Song, X. S. Wan, Y. Wang, W. L. Wang, Z. Wen, P. Xiu, J. Zhang, R. Zhang, K. Zhou, Upper ocean biogeochemistry of the oligotrophic north pacific subtropical gyre: From nutrient sources to carbon export. *Rev. Geophys.* **61**, e2022RG000800 (2023).
3. S. Meng, X. Gong, Y. Yu, X. Yao, X. Gong, K. Lu, C. Zhang, J. Shi, X. Yu, H. Gao, Strengthened ocean-desert process in the North Pacific over the past two decades. *Environ. Res. Lett.* **16**, 024034 (2021).
4. N. C. Harms, N. Lahajnar, B. Gaye, T. Rixen, U. Schwarz-Schampera, K. C. Emeis, Sediment trap-derived particulate matter fluxes in the oligotrophic subtropical gyre of the South Indian Ocean. *Deep. Res. II Top. Stud. Oceanogr.* **183**, 104924 (2021).
5. T. J. Pitcher, M. R. Clark, T. Morato, R. Watson, Seamount fisheries: Do they have a future? *Oceanography* **23**, 134–144 (2010).
6. T. Morato, D. A. Varkey, C. Damaso, M. Machete, M. Santos, R. Prieto, R. S. Santos, T. J. Pitcher, Evidence of a seamount effect on aggregating visitors. *Mar. Ecol. Prog. Ser.* **357**, 23–32 (2008).
7. M. R. Clark, A. A. Rowden, T. Schlacher, A. Williams, M. Consalvey, K. I. Stocks, A. D. Rogers, T. D. O'Hara, M. White, T. M. Shank, J. M. Hall-Spencer, The ecology of seamounts: Structure, function, and human impacts. *Ann. Rev. Mar. Sci.* **2**, 253–278 (2010).
8. A. D. Rogers, The biology of seamounts in *Advances in Marine Biology* (Elsevier Ltd., 1994), vol. 30, pp. 305–350.
9. A. D. Rogers, The biology of seamounts: 25 years on in *Advances in Marine Biology* (Elsevier Ltd., 2018), vol. 79, pp. 137–224.
10. T. Morato, S. D. Hoyle, V. Allain, S. J. Nicol, Seamounts are hotspots of pelagic biodiversity in the open ocean. *Proc. Natl. Acad. Sci. U.S.A.* **107**, 9707–9711 (2010).
11. J. W. Lavelle, C. Mohn, Motion, commotion, and biophysical connections at deep ocean seamounts. *Oceanography* **23**, 90–103 (2010).
12. A. B. Leitner, A. B. Neuheimer, J. C. Drazen, Evidence for long-term seamount-induced chlorophyll enhancements. *Sci. Rep.* **10**, 12729 (2020).
13. A. Genin, G. W. Boehlert, Dynamics of temperature and chlorophyll structures above a seamount: An oceanic experiment. *J. Mar. Res.* **43**, 907–924 (1985).
14. J. Dower, H. Freeland, K. Juniper, A strong biological response to oceanic flow past Cobb seamount. *Deep Sea Res. A Oceanogr. Res. Pap.* **39**, 1139–1145 (1992).
15. J. C. Vilas, J. Arístegui, K. Kiriakoulakis, G. A. Wolff, M. Espino, I. Polo, M. F. Montero, A. Mendonça, Seamounts and organic matter-Is there an effect? The case of Sedlo and Seine seamounts: Part 1. Distributions of dissolved and particulate organic matter. *Deep. Sea Res. II Top. Stud. Oceanogr.* **56**, 2618–2630 (2009).
16. C. Stevens, M. Consalvey, J. Devine, M. Clark, Mixing and transport near the shallow-crested Rumble III seamount and the implications for plankton distribution. *New Zeal. J. Mar. Freshw. Res.* **48**, 194–215 (2014).
17. J. Ma, J. Song, X. Li, Q. Wang, X. Sun, W. Zhang, G. Zhong, Seawater stratification vs. plankton for oligotrophic mechanism: A case study of M4 seamount area in the western Pacific Ocean. *Mar. Environ. Res.* **169**, 105400 (2021).
18. T. Nagai, D. Hasegawa, E. Tsutsumi, H. Nakamura, A. Nishina, T. Senjyu, T. Endoh, T. Matsuno, R. Inoue, A. Tandon, The Kuroshio flowing over seamounts and associated submesoscale flows drive 100-km-wide 100-1000-fold enhancement of turbulence. *Commun. Earth Environ.* **2**, 170 (2021).
19. P. J. Hosegood, W. A. M. Nimmo-Smith, R. Proud, K. Adams, A. S. Brierley et al., *Prog. Oceanogr.* **172**, 34–50 (2019).
20. X. Jiang, C. Dong, Y. Ji, C. Wang, Y. Shu, L. Liu, J. Ji, Influences of deep-water seamounts on the hydrodynamic environment in the northwestern Pacific Ocean. *J. Geophys. Res. Ocean.* **126**, e2021JC017396 (2021).
21. J. W. Lavelle, I. D. Lozovatsky, D. C. Smith IV, Tidally induced turbulent mixing at Irving seamount - Modeling and measurements. *Geophys. Res. Lett.* **31**, L10308 (2004).
22. R. G. Lueck, T. D. Mudge, Topographically induced mixing around a shallow seamount. *Science* **276**, 1831–1833 (1997).
23. L. A. Comeau, A. F. Vézina, M. Bourgeois, S. K. Juniper, Relationship between phytoplankton production and the physical structure of the water column near Cobb seamount, northeast Pacific. *Deep Sea Res. I Oceanogr. Res. Pap.* **42**, 993–1005 (1995).
24. S. Dai, Y. Zhao, X. Li, Z. Wang, M. Zhu, J. Liang, H. Liu, Z. Tian, X. Sun, The seamount effect on phytoplankton in the tropical western Pacific. *Mar. Environ. Res.* **162**, 105094 (2020).
25. S. Dai, Y. Zhao, X. Li, Z. Wang, M. Zhu, J. Liang, H. Liu, X. Sun, Seamount effect on phytoplankton biomass and community above a deep seamount in the tropical western Pacific. *Mar. Pollut. Bull.* **175**, 113354 (2022).
26. M. J. Sonnekus, T. G. Bornman, E. E. Campbell, Phytoplankton and nutrient dynamics of six South West Indian Ocean seamounts. *Deep. Sea Res. II Top. Stud. Oceanogr.* **136**, 59–72 (2017).
27. H. Demarcq, M. Noyon, M. J. Roberts, Satellite observations of phytoplankton enrichments around seamounts in the South West Indian Ocean with a special focus on the Walters Shoal. *Deep. Sea Res. II Top. Stud. Oceanogr.* **176**, 104800 (2020).
28. P. Afonso, N. McGinty, M. Machete, Dynamics of whale shark occurrence at their fringe oceanic habitat. *PLOS ONE* **9**, e102060 (2014).
29. L. Dubroca, E. Chassot, L. Floch, H. Demarcq, C. Assan, A. Delgado De Molina, Seamounts and tuna fisheries : Tuna hotspots or fishermen habits? *Collect. Vol. Sci. Rap. ICCAT* **69**, 2087–2102 (2014).
30. S. Samadi, L. Bottan, E. Macpherson, B. R. De Forges, M. C. Boisselier, Seamount endemism questioned by the geographic distribution and population genetic structure of marine invertebrates. *Mar. Biol.* **149**, 1463–1475 (2006).
31. A. Genin, J. F. Dower, Seamount plankton dynamics in *Seamounts: Ecology, Fisheries & Conservation* (Blackwell Publishing, 2007), pp. 87–100.
32. M. White, C. Mohn, *Seamounts: a review of physical processes and their influence on the seamount ecosystem*. (Oasis Rep., National University of Ireland, 2004).
33. C. R. Smith, F. C. De Leo, A. F. Bernardino, A. K. Sweetman, P. M. Arbizu, Abyssal food limitation, ecosystem structure and climate change. *Trends Ecol. Evol.* **23**, 518–528 (2008).
34. K. L. Smith, H. A. Ruhl, C. L. Huffard, M. Messié, M. Kahru, Episodic organic carbon fluxes from surface ocean to abyssal depths during long-term monitoring in NE Pacific. *Proc. Natl. Acad. Sci. U.S.A.* **115**, 12235–12240 (2018).
35. P. W. Boyd, H. Claustre, M. Levy, D. A. Siegel, T. Weber, Multi-faceted particle pumps drive carbon sequestration in the ocean. *Nature* **568**, 327–335 (2019).
36. K. L. Smith, H. A. Ruhl, B. J. Bett, D. S. M. Billett, R. S. Lampitt, R. S. Kaufmann, Climate, carbon cycling, and deep-ocean ecosystems. *Proc. Natl. Acad. Sci. U.S.A.* **106**, 19211–19218 (2009).
37. J. Hu, W. Zhuang, J. Zhu, Z. Huang, S. Chen, H. Peng, Temperature, Salinity and Water Mass in the South China Sea in *Regional Oceanography of the South China Sea* (World Scientific, 2020), pp. 43–75.
38. M. Nikurashin, R. Ferrari, Global energy conversion rate from geostrophic flows into internal lee waves in the deep ocean. *Geophys. Res. Lett.* **38**, L08610 (2011).
39. C. Du, Z. Liu, S.-J. Kao, M. Dai, Diapycnal fluxes of nutrients in an oligotrophic oceanic regime: The South China Sea. *Geophys. Res. Lett.* **44**, 11510–11518 (2017).
40. C. Du, Z. Liu, M. Dai, S. J. Kao, Z. Cao, Y. Zhang, T. Huang, L. Wang, Y. Li, Impact of the Kuroshio intrusion on the nutrient inventory in the upper northern South China Sea: Insights from an isopycnal mixing model. *Biogeosciences* **10**, 6419–6432 (2013).
41. J. J. Cullen, Subsurface chlorophyll maximum layers: Enduring enigma or mystery solved? *Ann. Rev. Mar. Sci.* **7**, 207–239 (2015).
42. J. Ma, J. Song, X. Li, H. Yuan, N. Li, L. Duan, Q. Wang, Environmental characteristics in three seamount areas of the tropical western Pacific Ocean: Focusing on nutrients. *Mar. Pollut. Bull.* **143**, 163–174 (2019).
43. B. Mouriño, E. Fernández, P. Serret, D. Harbour, B. Sinha, R. Pingree, Variability and seasonality of physical and biological fields at the Great Meteor Tablemount (subtropical NE Atlantic). *Oceanol. Acta* **24**, 167–185 (2001).
44. T. Odate, K. Furuya, Well-developed subsurface chlorophyll maximum near Komahashi No. 2 seamount in the summer of 1991. *Deep. Sea Res. I Oceanogr. Res. Pap.* **45**, 1595–1607 (1998).
45. S. Hernández-León, M. P. Olivar, M. L. Fernández de Puelles, A. Bode, A. Castellón, C. López-Pérez, V. M. Tuset, J. I. González-Gordillo, Zooplankton and micronekton active flux across the tropical and subtropical Atlantic Ocean. *Front. Mar. Sci.* **6**, 535 (2019).
46. O. Aumont, O. Maury, S. Lefort, L. Bopp, Evaluating the potential impacts of the diurnal vertical migration by marine organisms on marine biogeochemistry. *Global Biogeochem. Cycles* **32**, 1622–1643 (2018).
47. T. T. Packard, M. Gómez, Modeling vertical carbon flux from zooplankton respiration. *Prog. Oceanogr.* **110**, 59–68 (2013).

48. J. T. Turner, Zooplankton fecal pellets, marine snow, phytodetritus and the ocean's biological pump. *Prog. Oceanogr.* **130**, 205–248 (2015).
49. I. J. Alonso-Gonzalez, J. Aristegui, C. Lee, A. Sanchez-Vidal, A. Calafat, J. Fabres, P. Sangra, P. Masque, A. Hernandez-Guerra, V. Benitez-Barrios, Role of slowly settling particles in the ocean carbon cycle. *Geophys. Res. Lett.* **37**, L13608 (2010).
50. S. Hernández-León, R. Koppelmann, E. Fraile-Nuez, A. Bode, C. Mompeán, X. Irigoien, M. P. Olivar, F. Echevarría, M. L. F. de Puelles, J. I. González-Gordillo, A. Cózar, J. L. Acuña, S. Agustí, C. M. Duarte, Large deep-sea zooplankton biomass mirrors primary production in the global ocean. *Nat. Commun.* **11**, 6048 (2020).
51. B. Martin, B. Christiansen, Distribution of zooplankton biomass at three seamounts in the NE Atlantic. *Deep. Sea Res. II Top. Stud. Oceanogr.* **56**, 2671–2682 (2009).
52. A. Denda, B. Christiansen, Zooplankton distribution patterns at two seamounts in the subtropical and tropical NE Atlantic. *Mar. Ecol.* **35**, 159–179 (2014).
53. J. M. Gove, M. A. McManus, A. B. Neuheimer, J. J. Polovina, J. C. Drazen, C. R. Smith, M. A. Merrifield, A. M. Friedlander, J. S. Ehses, C. W. Young, A. K. Dillon, G. J. Williams, Near-island biological hotspots in barren ocean basins. *Nat. Commun.* **7**, 10581 (2016).
54. M. Messié, A. Petrenko, A. M. Doglioli, E. Martinez, S. Alvain, Basin-scale biogeochemical and ecological impacts of islands in the tropical Pacific Ocean. *Nat. Geosci.* **15**, 469–474 (2022).
55. R. Zhao, F. Zhao, L. Feng, J. K. H. Fang, C. Liu, K. Xu, A deep seamount effect enhanced the vertical connectivity of the planktonic community across 1,000 m above summit. *J. Geophys. Res. Ocean.* **128**, e2022JC018898 (2023).
56. T. Uchida, D. Balwada, R. P. Abernathey, G. A. McKinley, S. K. Smith, M. Lévy, Vertical eddy iron fluxes support primary production in the open Southern Ocean. *Nat. Commun.* **11**, 1125 (2020).
57. A. Oschlies, V. Garçon, Eddy-induced enhancement of primary production in a model of the North Atlantic Ocean. *Nature* **394**, 266–269 (1998).
58. J. H. Faghmous, I. Frenger, Y. Yao, R. Warmka, A. Lindell, V. Kumar, A daily global mesoscale ocean eddy dataset from satellite altimetry. *Sci. Data* **2**, 150028 (2015).
59. A. Lorrain, F. Houlbrèque, F. Benzoni, L. Barjon, L. Tremblay-Boyer, C. Menkes, D. P. Gillikin, C. Payri, H. Jourdan, G. Boussarie, A. Verheyden, E. Vidal, Seabirds supply nitrogen to reef-building corals on remote Pacific islets. *Sci. Rep.* **7**, 3721 (2017).
60. T. M. Shank, Seamounts: Deep-ocean laboratories of faunal connectivity, evolution, and endemism. *Oceanography* **23**, 108–122 (2010).
61. C. Garrigue, P. J. Clapham, Y. Geyer, A. S. Kennedy, A. N. Zerbini, Satellite tracking reveals novel migratory patterns and the importance of seamounts for endangered south pacific humpback whales. *R. Soc. Open Sci.* **2**, 150489 (2015).
62. Y. H. Park, J. H. Lee, I. Durand, C. S. Hong, Validation of Thorpe-scale-derived vertical diffusivities against microstructure measurements in the Kerguelen region. *Biogeosciences* **11**, 6927–6937 (2014).
63. A. Gargett, T. Garner, Determining Thorpe scales from ship-lowered CTD density profiles. *J. Atmos. Oceanic Tech.* **25**, 1657–1670 (2008).
64. T. M. Dillon, Vertical overturns: A comparison of Thorpe and Ozmidov length scales. *J. Geophys. Res.* **87**, 9601–9613 (1982).
65. T. Osborn, Estimates of the local rate of vertical diffusion from dissipation measurements. *J. Phys. Oceanogr.* **10**, 83–89 (1980).
66. M. Picheral, L. Guidi, L. Stemmann, D. M. Karl, G. Iddaoud, G. Gorsky, The underwater vision profiler 5: An advanced instrument for high spatial resolution studies of particle size spectra and zooplankton. *Limnol. Oceanogr. Methods* **8**, 462–473 (2010).
67. L. Guidi, G. A. Jackson, L. Stemmann, J. C. Miquel, M. Picheral, G. Gorsky, Relationship between particle size distribution and flux in the mesopelagic zone. *Deep. Sea Res. I Oceanogr. Res. Pap.* **55**, 1364–1374 (2008).
68. L. Guidi, S. Chaffron, L. Bittner, D. Eveillard, A. Larhlimi, S. Roux, Y. Darzi, S. Audic, L. Berline, J. R. Brum, L. P. Coelho, J. C. I. Espinoza, S. Malviya, S. Sunagawa, C. Dimier, S. Kandels-Lewis, M. Picheral, J. Poulain, S. Searson, L. Stemmann, F. Not, P. Hingamp, S. Speich, M. Follows, L. Karp-Boss, E. Boss, H. Ogata, S. Pesant, J. Weissenbach, P. Wincker, S. G. Acinas, P. Bork, C. De Vargas, D. Iudicone, M. B. Sullivan, J. Raes, E. Karsenti, C. Bowler, G. Gorsky, Plankton networks driving carbon export in the oligotrophic ocean. *Nature* **532**, 465–470 (2016).
69. R. Kiko, A. Biastoch, P. Brandt, S. Cravatte, H. Hauss, R. Hummels, I. Kriest, F. Marin, A. M. P. McDonnell, A. Oschlies, M. Picheral, F. U. Schwarzkopf, A. M. Thurnherr, L. Stemmann, Biological and physical influences on marine snowfall at the equator. *Nat. Geosci.* **10**, 852–858 (2017).
70. L. Guidi, L. Stemmann, G. A. Jackson, F. Ibanez, H. Claustre, L. Legendre, M. Picheral, G. Gorsky, Effects of phytoplankton community on production, size, and export of large aggregates: A world-ocean analysis. *Limnol. Oceanogr.* **54**, 1951–1963 (2009).
71. C. Yesson, T. B. Letessier, A. Nimmo-Smith, P. Hosegood, A. S. Brierley, M. Hardouin, R. Proud, Improved bathymetry leads to >4000 new seamount predictions in the global ocean – but beware of phantom seamounts! *UCL Open Environ.* **4**, 1–9 (2021).
72. B. Tozer, D. T. Sandwell, W. H. F. Smith, C. Olson, J. R. Beale, P. Wessel, Global bathymetry and topography at 15 arc sec: SRTM15+. *Earth Space Sci.* **6**, 1847–1864 (2019).
73. R. Kiko, M. Picheral, D. Antoine, M. Babin, L. Berline, T. Biard, E. Boss, P. Brandt, F. Carlotti, S. Christiansen, L. Coppola, L. De La Cruz, E. Diamond-Riquier, X. Durrieu De Madron, A. Elineau, G. Gorsky, L. Guidi, H. Hauss, J. O. Irisson, L. Karp-Boss, J. Karstensen, D. G. Kim, R. M. Lekanoff, F. Lombard, R. M. Lopes, C. Marec, A. M. P. Mcdonnell, D. Niemeyer, M. Noyon, S. H. O'daly, M. D. Ohman, J. L. Pretty, A. Rogge, S. Searson, M. Shibata, Y. Tanaka, T. Tanhua, J. Taucher, E. Trudnowska, J. S. Turner, A. Waite, L. Stemmann, A global marine particle size distribution dataset obtained with the underwater vision Profiler 5. *Earth Syst. Sci. Data* **14**, 4315–4337 (2022).
74. C. H. Lamborg, K. O. Buesseler, P. J. Lam, Sinking fluxes of minor and trace elements in the North Pacific Ocean measured during the VERTIGO program. *Deep. Sea Res. II Top. Stud. Oceanogr.* **55**, 1564–1577 (2008).
75. N. Yamada, H. Fukuda, H. Ogawa, H. Saito, M. Suzumura, Heterotrophic bacterial production and extracellular enzymatic activity in sinking particulate matter in the western North Pacific Ocean. *Front. Microbiol.* **3**, 379 (2012).
76. H. Li, M. G. Wiesner, J. Chen, Z. Ling, J. Zhang, L. Ran, Long-term variation of mesopelagic biogenic flux in the central South China Sea: Impact of monsoonal seasonality and mesoscale eddy. *Deep. Sea Res. I Oceanogr. Res. Pap.* **126**, 62–72 (2017).

Acknowledgments: We thank the Southern Marine Science and Engineering Guangdong Laboratory (Zhuhai) for the cruise support. We thank the crew of R/V *Shenkuo* for assistance in the deployment and recovery of the instruments. We thank J. Li (Guangdong Ocean University) and Z. Wang (Second Institute of Oceanography, MNR) for help in the field observations. **Funding:** This project was supported by the Natural Science Foundation of China grant no. 42330412 (J.C.), the National Key Research and Development Plan grant no. 2023YFF0805002 (H.L.), the Southern Marine Science and Engineering Guangdong Laboratory (Zhuhai) grant nos. SML2020SI1001 (W.X.) and SML2021SP207 (X.X.), and the Scientific Research Fund of the Second Institute of Oceanography, MNR grant no. SZ2403 (H.L.). **Author contributions:** Conceptualization: H.L. and J.C. Methodology: X.W., H.L., J.Z., and X.X. Investigation: X.W., X.X., W.X., and D.Z. Visualization: X.W., H.L., and J.Z. Supervision: H.L., J.Z., and J.C. Writing—original draft: X.W., H.L., and J.Z. Writing—review and editing: H.L., J.Z., J.C., K.Y., D.R.-P., and S.-J.K. **Competing interests:** The authors declare that they have no competing interests. **Data and materials availability:** All data needed to evaluate the conclusions in the paper are present in the paper and/or the Supplementary Materials. The data for this study have been deposited in the database dryad and https://doi.org/10.5061/dryad.rr4xgxdfx.

Submitted 8 September 2023
Accepted 17 May 2024
Published 26 June 2024
10.1126/sciadv.adk6833